Nano Research
2019, 12(12): 3089–3094

ISSN 1998-0124 CN 11-5974/O4
https://doi.org/10.1007/s12274-019-2556-8

Research Article

Controlled oxidation of Ni for stress-free hole transport layer of large-scale perovskite solar cells

Seongha Lee[1], Hee-Suk Roh[1], Gill Sang Han[2] (✉), and Jung-Kun Lee[1] (✉)

[1] *Department of Mechanical Engineering and Materials Science, University of Pittsburgh, Pennsylvania 15261, USA*
[2] *School of Advanced Materials Science and Engineering, Sungkyunkwan University, Suwon 16419, Republic of Korea*

Received: 12 July 2019 / **Revised:** 5 October 2019 / **Accepted:** 31 October 2019

ABSTRACT

The effect of the residual thermal stress of NiO films on the performance of an inverted type perovskite solar cell was studied. In this study, NiO films were grown on fluorine doped tin oxide (FTO) substrates of different surface roughness by thermally oxidizing Ni film and were tested as a hole transport layer for large-scale perovskite solar cells. Experimental and simulation results show that it is very important to suppress the appearance of the residual stress at the NiO–FTO interface during the oxidation of the Ni film for effective hole extraction. The Ni oxidation on the flat FTO film produced in-plane compressive stress in the NiO film due to the Ni film volume expansion. This led to the formation of defects including small blisters. These residual stress and defects increased leakage current through the NiO film, preventing holes from being selectively collected at the NiO-perovskite interface. However, when Ni was deposited and oxidized on the rough surface, the residual stress of the NiO film was negligible and its inherent high resistance was maintained. Stress-free NiO film is an excellent hole transport layer that stops the photogenerated electrons of the perovskite layer from moving to FTO. The improvements in the structural and electrical qualities of the NiO film by engineering the residual stress reduce the carrier recombination and increase the power conversion efficiency of the perovskite solar cells to 16.37%.

KEYWORDS

nickel oxidation, surface roughness, residual stress, perovskite solar cells, large scale processing

1 Introduction

Developments in organometal halide perovskite solar cells (PSCs) over the last 5 years have provided very fast improvements in the power conversion efficiency (PCE). In addition to the PCE improvements, one of the important research subjects in PSCs is to fabricate more stable and reliable devices. To meet this need, extensive research on the device structure, material processing, and physical and electrical properties are currently underway [1]. Depending on the carrier transport direction, the device structures of PSCs are classified as normal or inverted [2–5]. While planar normal PSCs consisting of a TiO_2 electron transport layer (ETL) and Sprio-OMeTAD hole transport layer (HTL) exhibit a higher PCE, there are several associated issues, such as large hysteresis, photocatalytic dissociations, and instabilities of additives in HTL [6–8]. The inverted PSCs with NiO HTLs and phenyl-C61-butyric acid methyl ester (PCBM) ETLs can be used to address these problems by the removal of TiO_2 ETLs and the employment of a stable oxide hole conductor [9–11].

Compared to polymer p-type semiconductors poly(3,4-ethylenedioxythiophene)-poly(styrene sulfonate) (PEDOT:PSS), NiO*x* (NiO) has a high transparency (*Eg*: 3.6–4.0 eV), good hole mobility, suitable work function, excellent stability, and effective electron blocking ability in PSCs [12, 13]. To date, the solution process is widely used for inverted PSCs due to its simple process and compatibility with flexible devices. However, NiO films obtained from the solution process are composed of tiny NiO nanoparticles, which can cause inefficient electron blocking and poor hole transport [14–16]. In addition, it is difficult to deposit uniform NiO films on large substrates by the solution process [17]. Therefore, several techniques, such as e-beam deposition, sputtering, atomic layer deposition, and pulsed laser deposition, have been tested for high quality NiO film depositions [18–23].

In this study, we investigated the thermal oxidation of e-beam deposited Ni films for stress-free highly crystalline NiO films, which can be applied to the fabrication of large-scale inverted PSCs. The volume expansion during the conversion of Ni to NiO induces compressive residual stress, producing extended defects and the deterioration of the performance of NiO as the HTL [24]. To mitigate the occurrence of NiO residual stress, the surface roughness effect of fluorine doped SnO_2 (FTO) underlying a Ni film was studied. Experimental and simulation results showed that an increase in the surface roughness of the FTO reduced the residual stress of NiO. Inverted PSCs with a thermally oxidized NiO film exhibited a PCE of 16.37%, with a short-circuit current (J_{SC}) of 21.5 mA/cm^2, open circuit voltage (V_{OC}) of 1.04 V, and fill factor (FF) of 0.73. Moreover, the oxidized NiO film was deposited uniformly on a large-scale substrate, which is applicable to the future large-scale manufacture of PSCs.

2 Experimental

2.1 Preparation of NiO films

Ni films of thickness 20, 30, and 50 nm were deposited on two different FTO coated glasses (TEC8 and TEC15 from Pilkington) by e-beam evaporation. The surface roughness of the FTO layers

Address correspondence to Gill Sang Han, hangillsang1@gmail.com; Jung-Kun Lee, jul37@pitt.edu

were 24.8 and 4.98 nm for the TEC8 and TEC15, respectively. The samples were labelled to represent the thickness of the Ni film (20Ni or 30Ni) and the type of FTO coated glass (T8 or T15), i.e., 20Ni/T8 and 20Ni/T15 refer to 20 nm thick Ni films on TEC8 and TEC15, respectively, and 30Ni/T8 and 30Ni/T15 refer to 30 nm thick Ni films on TEC8 and TEC15, respectively. The FTO coated glasses were cut into square pieces, 20 mm × 20 mm × 0.025 mm, and partially etched using zinc powder and hydrochloric acid (2 M) before the Ni deposition. The substrates were then sequentially cleaned by acetone, deionized (DI) water, and ethanol for 30 min. After Ni film deposition, the Ni/FTO samples were annealed at 550 °C for 6 h in air to form an NiO layer at the top of the FTO.

2.2 Fabrication of the PSCs

Inverted PSCs with FTO/NiO/$CH_3NH_3PbI_3$/PCBM/BCP/Ag structures were fabricated by the following sequence. After the Ni film was deposited and oxidized on the FTO/glass substrates, a perovskite ($CH_3NH_3PbI_3$) layer was deposited by the adduct method, as reported previously [5]. The $CH_3NH_3PbI_3$ solution was prepared by dissolving lead iodide (PbI_2), methyl ammonium iodide (MAI, CH_3NH_3I), and dimethyl sulfoxide (DMSO) with a molar ratio of 1:1:1 in N,N-dimethylformamide (DMF). This solution was spin-coated on top of the NiO/FTO at 4,000 rpm for 25 s, while slowly dropping 0.5 mL of diethyl ether. The spin-coated samples were annealed at 60 °C, and then at 100 °C for 1 and 5 min, respectively. The PCBM layer was deposited on the perovskite layer by the spin-coating of PCBM (20 mg) dissolved in dichlorobenzene (1 mL) at 2,000 rpm for 60 s. Subsequently, 5 mg of BCP in ethanol (10 mL) was spin-coated on the PCBM layer at 4,000 rpm for 40 s. Finally, an 80-nm-thick Ag electrode was deposited by thermal evaporation at ~10^{-6} bar through a shadow mask. A deposition rate of Ag electrode is 0.5 Å/s.

2.3 Characterization

The crystal structure of the NiO film was obtained by X-ray diffraction (XRD; X'Pert, PANalytical). The surface morphology and cross-sectional view of the samples were examined using a field-emission scanning electron microscope (FESEM; XL-30F, Phillps FEI) and atomic force microscope (AFM, MV-1000, Nanonics). The ultraviolet–visible (UV–vis) transmittance spectra of the NiO films were recorded with a UV–vis spectrometer equipped with an integrating sphere (Lambda35, PerkinElmer). The indentation analysis (Hysitron TriboLab®, Nanomechanical Test Instrument) was conducted with a Berkovich diamond indenter at room temperature. An electrochemical workstation (CHI660, CHI Instrument) system was utilized to obtain the photovoltaic performances of the PSCs. A solar simulator (Oriel Sol 3A class AAA, Newport) was used as a light source, calibrated for the AM 1.5 G condition for a reference Si solar cell (PVM 95). The effective area of the PSCs was defined as 0.14 cm^2 using a non-reflective metal mask.

3 Results and discussion

3.1 Crystal structure, microstructure and optical properties of oxidized Ni films

The Ni films were deposited on the FTO substrates with different surface roughness (TEC15 and TEC8) by e-beam evaporation. TEC8 was chosen as the rough surface FTO substrate (surface roughness: 24.8 nm), while the TEC15 had a relatively flat surface (surface roughness: 4.98 nm). The Ni films were thermally oxidized at 550 °C for 6 h in air to form the NiO films. Since the oxygen diffusion coefficient of Ni film is 9.4 × 10^{-14} cm^2/s at 550 °C, 6 h is long enough to fully oxidize 30 nm thick Ni film as well as 20 nm thick Ni film [25]. Figure 1(a) shows the grazing incidence X-ray diffraction (GIXRD) patterns of Ni on the FTO substrate, before and after oxidation. A peak at 44.7° was indexed as the (111) planes of Ni with a face centered cubic structure. After the oxidation, the two main peaks at 2θ of 37.2° and 43.2° are indexed as the (111) and (200) planes of cubic NiO. Disappearance of Ni phase peak in the oxidized film indicates that Ni was completely oxidized into NiO by the thermal treatment at 550 °C for 6 h in air. Figure 1(c) shows the cross-sectional SEM image of the Ni film on the TEC8 FTO substrate. The thickness of Ni was approximately 20 nm. Figure 1(d) shows the thickness of the NiO film was expanded to ~ 43 nm after the oxidation. Since the weight of the film increases by 127% during the transition from Ni to NiO and the theoretical densities of Ni and NiO are 8.91 and 6.67 g/cm^3, the volume of the oxidized NiO is approximately 1.70 times greater than that of the initial Ni film at room temperature. In addition, the mechanical constraint of the substrate restricts the expansion along the plane direction and the NiO film has additional expansion in parallel to the film thickness direction. By considering Poisson's ratio of NiO, which is 0.3 [26, 27], the total thickness of the NiO film is calculated to be 2.21 times greater than that of Ni. The experimental NiO thickness from the oxidation of 20 and 30 nm thick Ni films was 2.05 and 2.14 times than that of Ni, which agrees well with the theoretical value. Figure 1(e) shows the optical transmittance spectra of the NiO films on different FTO glass substrates. The average transmittances (T_{ave}) of NiO in the wavelength range 400 to 800 nm were 79.0 and 83.8 for the oxidized 20Ni/T8 (20 nm thick Ni film on TEC8) and the oxidized 20Ni/T15 (20 nm thick Ni film on TEC15), respectively. Figure 1(e) shows less light scattering of 20Ni/T15 for the shorter wavelength light and exhibits a slightly higher transmittance at the wavelength of 400–600 nm than 20Ni/T8. This is attributed to a smaller roughness

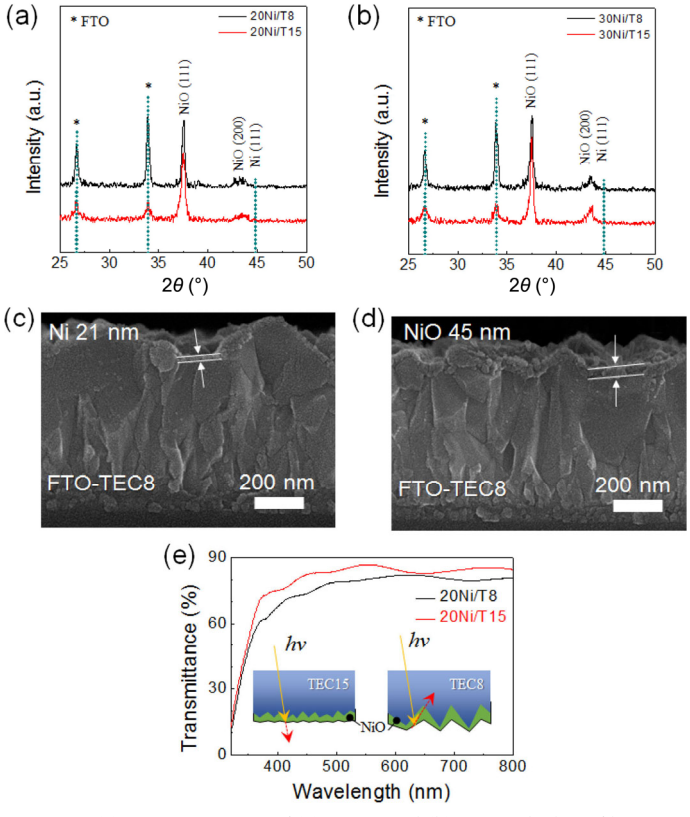

Figure 1 (a) GIXRD patterns of (a) 20 nm and (b) 30 nm thick Ni film on an FTO substrate before and after thermal oxidation. The Ni film was oxidized at 550 °C for 6 h in air. The cross-sectional SEM images of (c) as-deposited 20 nm thick Ni film on a TEC8 FTO substrate and (d) after the oxidization of 20 nm thick Ni film at 550 °C for 6 h in air. (e) UV–vis transmittance spectra of NiO*x* films formed by oxidizing the 20 nm Ni films on the TEC8 and TEC15 FTO substrates.

of 20Ni/T15 which is found in Fig. S1 in the Electronic Supplementary Material (ESM) [28, 29].

3.2 Surface roughness effect on the photovoltaic, electric and structural properties

Figure 2(a) shows representative *J*–*V* curves of inverted PSCs using NiO films which were converted from 20 nm thick Ni films on TEC8 and TEC15 (20Ni/T8 and 20Ni/T15). Table S1 in the ESM shows the device performance parameters of the PSCs. The 20Ni/T8 based PSCs exhibited the best performance; J_{SC} = 21.5 mA/cm^2, V_{OC} = 1.04 V, FF = 0.73, and PCE = 16.37%. Interestingly, although the 20Ni/T15 film had a higher transmittance than that of the 20Ni/T8 film, the device performance of 20Ni/T15 was worse than that of 20Ni/T8. In addition, Fig. 2(b) shows that the PSCs using thermally grown NiO film (20Ni/T8) were very reliable. The deviation of the PCEs was much less in the PSCs of the thermally grown NiO film, compared to that in the previously reported PSCs of the spin coated NiO nanoparticle film [14–16, 22]. This indicates that the NiO film formed by the oxidation of the Ni film was more uniform and reproducible than the NiO film formed by the spin-coating of NiO nanoparticles. Figure 2(a) also shows that both 20Ni/T8 and 20Ni/T15 samples did not exhibit any hysteresis in the *J*–*V* curve. In addition, Fig. S2 in the ESM shows large NiO/FTO/glass substrates (8 cm × 8 cm) and PCEs of solar cells (2 cm × 2 cm) using different parts of large NiO/FTO/glass substrate. A small variation of PCE suggests that thermally oxidized NiO film is suitable for fabricating large scale PSCs.

Since the fabrication process for the samples (20Ni/T8 and 20Ni/T15) was the same, except for surface roughness of the FTO, the electrical properties of the NiO films were investigated to determine the origins of the differences of the PCEs of the inverted PSCs. Figure 2(c) shows that the NiO films on the rough surface have the higher resistance than that of NiO films on smooth surface. To further investigate the mechanisms underlying the effect of the surface roughness of the substrates on the electric resistance of the NiO films, we examined the microstructures of the NiO films on TEC8 and TEC15. Scanning electron microscopy (SEM) images in Fig. 2(d) show that the microstructure of the NiO film on TEC8 is dense and uniform. On the other hand, Fig. 2(e) shows that blisters with a hemispherical morphology (indicated by a yellow arrow in the SEM images) are formed in the NiO film on TEC15. This blistering produces extended defects in NiO film and increases the leakage current. Therefore, the NiO film on TEC 15 does not work well as the HTL and deteriorates the performance of inverted PSCs. The formation of blisters and its effect on the electric property of NiO film are explained in detail in a next section.

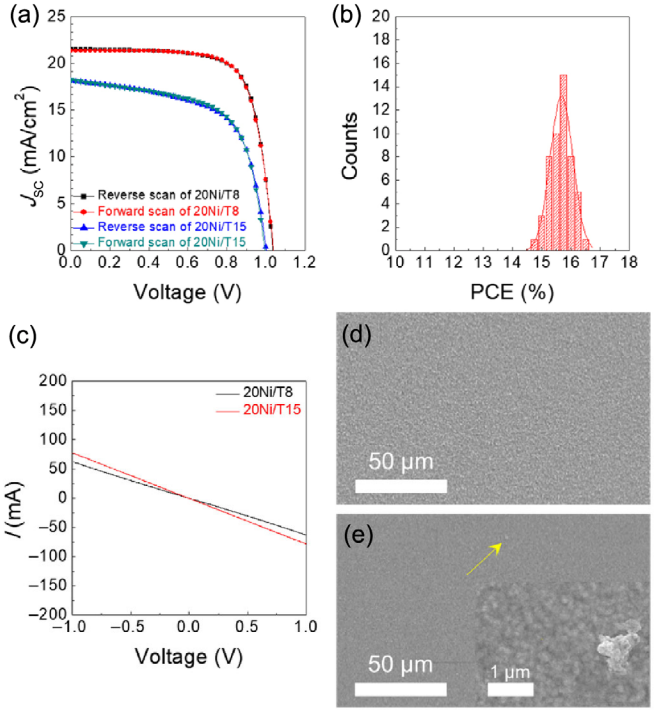

Figure 2 (a) *J*–*V* curves of the FTO/NiO/$CH_3NH_3PbI_3$/PCBM/BCP/Ag based PSCs obtained by reverse and forward scans for illumination with the AM 1.5 G condition, and 20 nm thickness Ni films on different FTO substrates after oxidizing. (b) Histogram of the 20Ni/T8 based PSCs. (c) Corresponding resistances of 20Ni/T8 and 20Ni/T15 in air. The measured device structure was FTO/NiO/Au Plan-view SEM images of the oxidized NiO films on TEC8 and TEC15: (c) 20Ni/T8, (d) 20Ni/T15 after oxidation in air.

3.3 Further examination of surface roughness effect using thicker NiO film

In section 3.2, the type of FTO substrate has a significant impact on the resistance and *I*–*V* characteristics of the oxidized NiO film. To further examine the effect of the surface roughness, another set of experiment was performed using thicker NiO films. Figure 3(a) shows representative *I*–*V* curves of inverted PSCs using different NiO films (30Ni/T8 and 30Ni/T15) which were converted from 30 nm thick Ni film. Compared with *I*–*V* curves of Fig. 2(a), the effect of the surface roughness is more clearly observed in *J*–*V* curves of 30Ni/T8 and 30Ni/T15. As shown in Table S1 in the ESM, PSCs of 30Ni/T8 have 4 times larger PCE than PSCs of 30Ni/T15. Overall incident photon-to-electron conversion efficiency (IPCE) spectra of PSCs are shown in Fig. S3 in the ESM. Electric resistance in Fig. 3(b) indicates that a large difference in PCE of PSCs is due to a dependence of the electric resistance on the surface roughness. 30Ni/T8 is much more resistive than 30Ni/T15.

When Fig. 3(b) is compared with Fig. 2(c), it is noted that the thicker NiO film from 30Ni/T15 has lower resistance than the thinner NiO film from 20Ni/T15. Given that an increase in the oxide thickness generally increases the electric resistance, an inverse relation between the thickness and the resistance of NiO films on TEC15 needs to be explained. While no blisters are found in NiO film on TEC8 (Fig. 3(c)), an increase in the thickness of NiO film on TEC15 increases a density of blisters and their radii. To understand the thickness effect on TEC15, 50 nm thick Ni film was oxidized and the microstructure of 100 nm thick NiO film was examined. Figure S4 in the ESM shows the plan-view and cross-section SEM images of 100 nm thick NiO film from TEC 15. It clearly confirms that an increase in the film thickness increases the size of the blisters and even induces partial delamination of NiO film on TEC 15. It is well-known that the volume expansion during the oxidation of metal thin films on rigid substrates leaves compressive residual stress in the metal oxide films [24]. If an increase in the metal film thickness increases the magnitude of the compressive residual stress beyond a certain limit, the buckling of the oxide films on the rigid substrates occurs and the blistering is promoted [30]. Experimental observations in Figs. 2(d), 2(e), 3(c), and 3(d) suggest that the smoother surface of TEC15 increases compressive residual stress in NiO film and an increase in the film thickness increases the magnitude of the residual stress. Extended defects such as dislocations and blisters appear more frequently in such films of higher residual stress, because the residual stress accelerates the diffusion of point defects and promotes the agglomeration of defects [31, 32]. These extended defects tend to increase the leakage current of semiconductors [33, 34], which explains why NiO films from 30Ni/T15 have the lower resistance than NiO films from 20Ni/T15. An increase in the leakage current, in turn, decreases the fill factor and PCE of solar cells by decreasing shunt resistance [35].

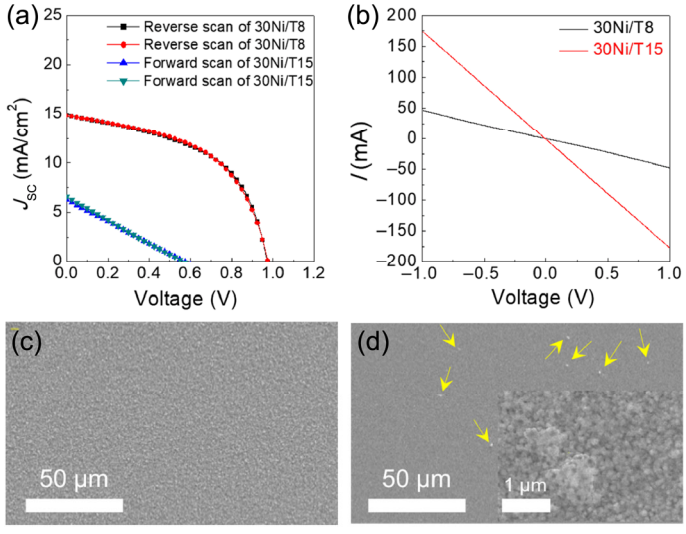

Figure 3 (a) *J*–*V* curves of the FTO/NiO/$CH_3NH_3PbI_3$/PCBM/BCP/Ag based PSCs obtained by reverse and forward scans for illumination with the AM 1.5 G condition, and 30 nm thickness Ni films on different FTO substrates after oxidizing. (b) Corresponding resistances of 30Ni/T8 and 30Ni/T15 in air. The measured device structure was FTO/NiO/Au. Plan-view SEM images of the oxidized NiO films on TEC8 and TEC15: (c) 30Ni/T8, (d) 30Ni/T15 after oxidation in air.

3.4 Characterization of residual stress

To examine the evolution of the residual compressive stress in the NiO film, the hardness of the NiO films was measured using the nanoindentation method. As the compressive stress prevents the propagation of cracks and increases the hardness [36], the nanoindentation is a good tool to characterize the status of the residual stress in materials. Figures 4(a) and 4(b) show the load-displacement curves of the 20 and 30 nm NiO films on different FTO substrates. The same load is applied for the NiO film of the same thickness and the penetration depth is controlled to be less than 1/3 of the film thickness [37]. The hardness of the NiO films was calculated by [38]

$$H = \frac{P_{max}}{A} \quad (1)$$

where H is the hardness, P_{max} is the maximum applied load and A is the projected contact area of an indent. Figure S5 in the ESM shows that the hardness of the Ni films before oxidation was almost same for 20Ni/T8 (1.11 GPa) and 20Ni/T15 (1.23 GPa) [39]. Similar hardness values were observed for the Ni films from 30Ni/T8 and 30Ni/T15.

However, after oxidation, the NiO films exhibit very different hardness. Figures 4(a) and 4(b) show that even though a same load was applied, the penetration depth of the NiO film on the rough surface (TEC8) was larger than that on the smooth surface (TEC15). Equation (1) shows that the NiO film from the 20Ni/T15 has a greater hardness (2.88 Gpa) than that from the 20Ni/T8 substrate (2.37 Gpa). The effect of the surface roughness on the hardness of NiO films is more clearly observed in the thicker NiO film. The hardness of NiO films was increased to 4.01 GPa (30Ni/T15) and 2.60 Gpa (Ni30/T8). These hardness values in this study are comparable with that of nanoscale NiO films [40]. The larger hardness of the NiO film on TEC 15 is attributed to larger compressive stress which is developed when Ni film on the flat surface is oxidized [30]. An increase in the film thickness increases the compressive stress, which forms blisters in NiO films and causes delamination at NiO-FTO interface.

Figure 5 shows Raman spectrum of NiO films. Rougher surface of TEC8 increases the width and intensity of Raman peak at ~ 570 cm^{-1} which is assigned to the first-order one-phonon (1P) longitudinal optical (LO) mode of NiO [41]. The first order 1P LO Raman peak

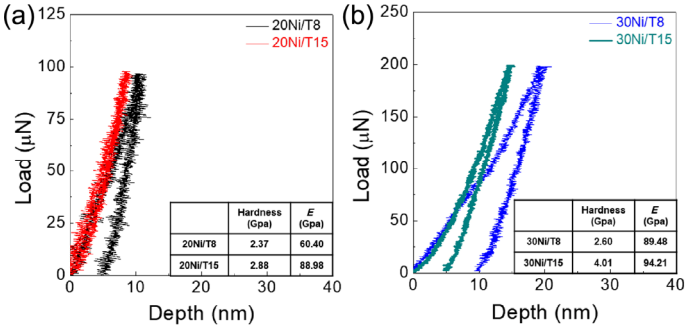

Figure 4 Load-displacement curves of the nanoindentation analysis for (a) 20 and (b) 30 nm Ni thick films on the TEC8 and TEC15 substrate, after oxidation at 550 °C for 6 h.

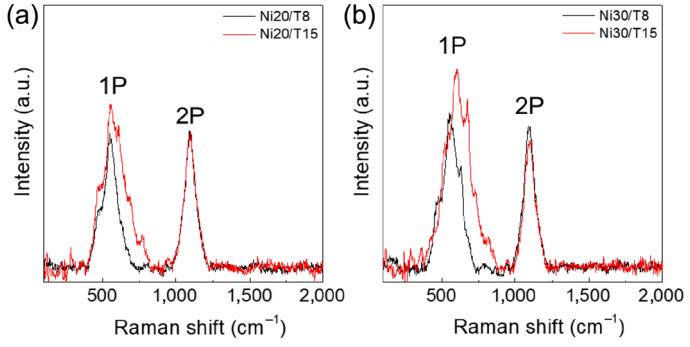

Figure 5 Representative Raman spectra and XRD spectra for (a) 20 nm and (b) 30 nm thickness Ni films on different FTO substrates after oxidizing at 550 °C for 6 h.

results from symmetry-breaking imperfections and an increase in the imperfection density increases its full width half maximum (FWHM). A peak at ~1,090 cm^{-1} corresponds to the second-order two-phonon (2P) 2LO mode and its FWHM is proportional to Bose-Einstein thermal factor. Since all measurements were done at room temperature, a negligible change is observed in 2P LO Raman peak that is sensitive to temperature. However, 1P peak of 20Ni/T15 is much broader than that of 20Ni/T8. This suggests that 20Ni/T15 has more compressive stress and resultant defects than 20Ni/T8. In 30Ni/T8 and 30Ni/T15, not only FWHM but also the peak position changes. An increase in Raman shift of 30Ni/T15 1P peak from ~550 to ~600 cm^{-1} indicates the development of high compressive stress in thicker NiO films [42]. Raman spectra confirm that the surface roughness affects the compressive residual stress of the NiO films and thicker NiO film on smoother substrates (30Ni/T15) has the largest compressive stress.

3.5 Computational simulation on the origin of residual stress

The experimentally measured differences in the compressive stress of the NiO films are theoretically verified using the finite element method. The evolution of the stress and strain of the NiO films on two different FTO substrates was simulated by ANSYS. The calculation is carried out on the assumption that the volume expansion during the oxidation of Ni is prohibited at the interface between the Ni layer and the FTO layer. The stiffness of the NiO films used in the calculation was 89.48 GPa (on TEC8) and 94.12 GPa (TEC15) which were obtained by the nanoindentation. Figures 6(a) and 6(b) show the calculation results of the compressive stress distributions of the NiO films with smooth and rough surfaces. The addition of oxygen into the constrained Ni films resulted in the NiO films of in-plane compressive stress and out-of-plane tensile strain. The volume of the Ni layer was expected to increase during the oxidation, since oxygen was added to the Ni film and the density of NiO is less than that of Ni. While the NiO layer expanded freely along the normal

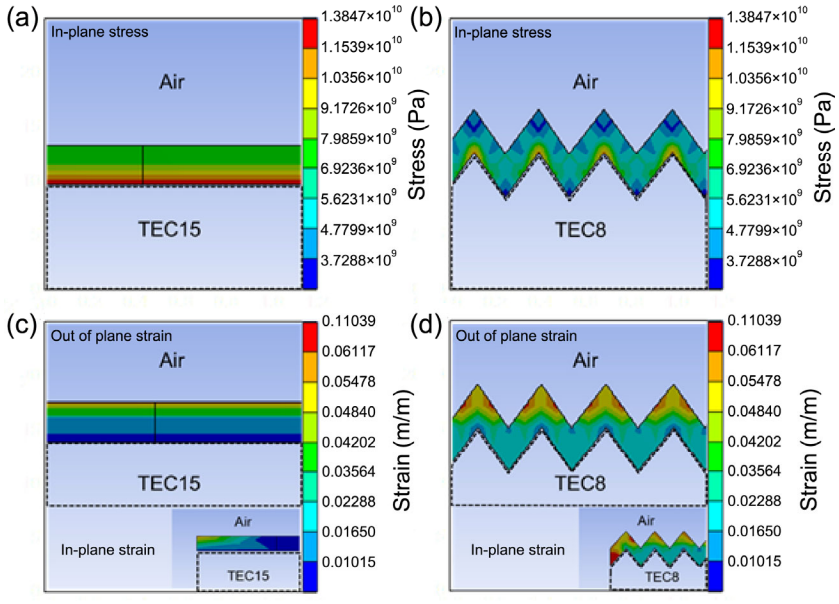

Figure 6 Calculated stress distributions of the NiO films after the oxidation process: on (a) flat and (b) rough surfaces. Calculated strain distributions of the NiO films after oxidation process: on (c) flat and (d) rough surface.

direction of the substrate, the rigid FTO substrate constrained the expansion of NiO layer along the in-plane direction, causing compressive stress in the NiO layer. Figure 6 shows that the maximum in-plane compressive stress of 13.8 GPa is uniformly applied to the bottom part of the NiO film on the flat surface. On the rough surface, the in-plane compressive stress of NiO film decreased significantly. The maximum compressive stress of NiO film on the rough surface was only 9.8 GPa, which was locally concentrated in the apex region of the NiO-FTO interface. Figures 6(c) and 6(d) show that a larger out-of-plane strain was produced in the NiO layer on the rough surface. This larger strain in the NiO layer on the rough surface relieves the stress, leading to the smaller compressive stress.

The simulation results demonstrate that the rough surface of FTO layer releases the compressive stress of the NiO film more effectively by allowing a higher volume expansion during the oxidation process. In contrast, the compressive stress is developed in NiO film on smoother substrate. As the film thickness increases, higher stress is built up near the NiO-FTO interface and a probability of forming extended defects increases. This suggests that the electron blocking ability of thermally oxidized NiO as a HTL of the PSCs depend on the surface roughness of the FTO and initial thickness of the Ni film.

4 Conclusion

We systematically studied the electric and mechanical properties of NiO using thermal oxidation, and its effect on the selective hole transport behavior as HTLs of inverted PSCs. When the surface roughness of substrates underlying the Ni film was higher, the thermally oxidized NiO film was more electrically resistive, had less in-plane compressive stress, and provided a better HTL performance. This is due to the evolution of greater out-of-plane strain and the formation of less extended defects. The Ni film on the smooth surface substrate produced more in-plane compressive stress, leading to the formation of extended defects, local blistering, and delamination of the NiO film. As a result, the leakage current of the NiO film increased, and the NiO layer in the inverted PSCs did not effectively block electrons. This result provides a guideline for designing uniform and high-quality NiO films on large substrates, which can be applied to the large-scale manufacturing of PSCs.

Acknowledgements

This work was supported from the Global Frontier R&D Program on Center for Multiscale Energy System, Republic of Korea (No. 2012M3A6A7054855) and National Science Foundation (NSF 1709307).

Electronic Supplementary Material: Supplementary material (device properties of the PCSs fabricated on different FTO substrates with different Ni thicknesses, representative atomic force microscopy images on different FTO with 20 nm thick Ni films before/after annealing at 550 °C for 6 h, PCE of solar cells using different parts of large NiO/FTO/glass substrate, SEM images of 100 nm thick NiO film on a TEC15 substrate, load-displacement curves from the nanoindentation analysis for the as-deposited 20 nm thick Ni film (before the oxidation process) on FTO, IPCE of different NiO/FTO/glass substrates) is available in the online version of this article at https://doi.org/10.1007/s12274-019-2556-8.

References

[1] Leblebici, S. Y.; Leppert, L.; Li, Y. B.; Reyes-Lillo, S. E.; Wickenburg, S.; Wong, E.; Lee, J.; Melli, M.; Ziegler, D.; Angell, D. K. et al. Facet-dependent photovoltaic efficiency variations in single grains of hybrid halide perovskite. *Nat. Energy* **2016**, *1*, 16093.

[2] Kim, H. S.; Lee, C. R.; Im, J. H.; Lee, K. B.; Moehl, T.; Marchioro, A.; Moon, S. J.; Humphry-Baker, R.; Yum, J. H.; Moser, J. E. et al. Lead iodide perovskite sensitized all-solid-state submicron thin film mesoscopic solar cell with efficiency exceeding 9%. *Sci. Rep.* **2012**, *2*, 591.

[3] Jeon, N. J.; Noh, J. H.; Kim, Y. C.; Yang, W. S.; Ryu, S.; Seok, S. I. Solvent engineering for high-performance inorganic–organic hybrid perovskite solar cells. *Nat. Mater.* **2014**, *13*, 897–903.

[4] Burschka, J.; Pellet, N.; Moon, S. J.; Humphry-Baker, R.; Gao, P.; Nazeeruddin, M. K.; Grätzel, M. Sequential deposition as a route to high-performance perovskite-sensitized solar cells. *Nature* **2013**, *499*, 316–319.

[5] Ahn, N.; Son, D. Y.; Jang, I. H.; Kang, S. M.; Choi, M.; Park, N. G. Highly reproducible perovskite solar cells with average efficiency of 18.3% and best efficiency of 19.7% fabricated via Lewis base adduct of lead(II) iodide. *J. Am. Chem. Soc.* **2015**, *137*, 8696–8699.

[6] Chen, B.; Yang, M. J.; Priya, S.; Zhu, K. Origin of *J*–*V* hysteresis in perovskite solar cells. *J. Phys. Chem. Lett.* **2016**, *7*, 905–917.

[7] Han, G. S.; Shim, H. W.; Lee, S.; Duff, M. L.; Lee, J. K. Low-temperature modification of ZnO nanoparticles film for electron-transport layers in

perovskite solar cells. *ChemSusChem* **2017**, *10*, 2425−2430.
[8] Han, G. S.; Yoo, J. S.; Yu, F. D.; Duff, M. L.; Kang, B. K; Lee, J. K. Highly stable perovskite solar cells in humid and hot environment. *J. Mater. Chem. A* **2017**, *5*, 14733−14740.
[9] Heo, J. H.; Han, H. J.; Kim, D.; Ahn, T. K.; Im, S. H. Hysteresis-less inverted $CH_3NH_3PbI_3$ planar perovskite hybrid solar cells with 18.1% power conversion efficiency. *Energy Environ. Sci.* **2015**, *8*, 1602–1608.
[10] Norrman, K.; Madsen, M. V.; Gevorgyan, S. A.; Krebs, F. C. Degradation patterns in water and oxygen of an inverted polymer solar cell. *J. Am. Chem. Soc.* **2010**, *132*, 16883–16892.
[11] Jørgensen, M.; Norrman, K.; Krebs, F. C. Stability/degradation of polymer solar cells. *Sol. Eng. Mater. Sol. Cells* **2008**, *92*, 686–714.
[12] Kwon, U.; Kim, B. G.; Nguyen, D. C.; Park, J. H.; Ha, N. Y.; Kim, S. J.; Ko, S. H.; Lee, S.; Lee, D.; Park, H. J. Solution-processible crystalline NiO nanoparticles for high-performance planar perovskite photovoltaic cells. *Sci. Rep.* **2016**, *6*, 30759.
[13] Wang, K. C.; Jeng, J. Y.; Shen, P. S.; Chang, Y. C.; Diau, W. G. G.; Tsai, C. H.; Chao, T. Y.; Hsu, H. C.; Lin, P. Y.; Chen, P. et al. P-type mesoscopic nickel oxide/organometallic perovskite heterojunction solar cells. *Sci. Rep.* **2014**, *4*, 4756.
[14] Yin, X. T.; Guo, Y. X.; Xie, H. X.; Que, W. X.; Kong, L. B. Nickel oxide as efficient hole transport materials for perovskite solar cells. *Sol. RRL* **2019**, *3*, 1900001.
[15] Yin, X. T.; Que, M. D.; Xing, Y. L.; Que, W. X. High efficiency hysteresis-less inverted planar heterojunction perovskite solar cells with a solution-derived NiO_x hole contact layer. *J. Mater. Chem. A* **2015**, *3*, 24495–24503.
[16] Yin, X. W.; Yao, Z. B.; Luo, Q.; Dai, X. Z.; Zhou, Y.; Zhang, Y.; Zhou, Y. Y.; Luo, S. P.; Li, J. B.; Wang, N. et al. High efficiency inverted planar perovskite solar cells with solution-processed NiO_x hole contact. *ACS Appl. Mater. Interfaces* **2017**, *9*, 2439–2448.
[17] Eperon, G. E.; Burlakov, V. M.; Docampo, P.; Goriely, A.; Snaith, H. J. Morphological control for high performance, solution-processed planar heterojunction perovskite solar cells. *Adv. Funct. Mater.* **2014**, *24*, 151–157.
[18] Li, G. J.; Jiang, Y. B.; Deng, S. B.; Tam, A.; Xu, P.; Wong, M.; Kwok, H. S. Overcoming the limitations of sputtered nickel oxide for high-efficiency and large-area perovskite solar cells. *Adv. Sci.* **2017**, *4*, 1700463.
[19] Peng, Y. Y.; Cheng, Y. D.; Wang, C. H.; Zhang, C. J.; Xia, H. Y.; Huang, K. Q.; Tong, S. C.; Hao, X. T.; Yang, J. L. Fully doctor-bladed planar heterojunction perovskite solar cells under ambient condition. *Org. Electron.* **2018**, *58*, 153–158.
[20] Wang, T.; Ding, D.; Wang, X.; Zeng, R. R.; Liu, H.; Shen, W. Z. High-performance inverted perovskite solar cells with mesoporous NiO_x hole transport layer by electrochemical deposition. *ACS Omega* **2018**, *3*, 18434−18443.
[21] Seo, S.; Park, I. J.; Kim, M.; Lee, S.; Bae, C.; Jung, H. S.; Park, N. G.; Kim, J. Y.; Shin, H. An ultra-thin, un-doped NiO hole transporting layer of highly efficient (16.4%) organic–inorganic hybrid perovskite solar cells. *Nanoscale* **2016**, *8*, 11403–11412.
[22] Pae, S. R.; Byun, S.; Kim, J.; Kim, M.; Gereige, I.; Shin, B. Improving uniformity and reproducibility of hybrid perovskite solar cells via a low-temperature vacuum deposition process for NiO_x hole transport layers. *ACS Appl. Mater. Interfaces* **2018**, *10*, 534−540.
[23] Park, J. H.; Seo, J.; Park, S.; Shin, S. S.; Kim, Y. C.; Jeon, N. J.; Shin, H. W.; Ahn, T. K.; Noh, J. H.; Yoon, S. C. et al. Efficient $CH_3NH_3PbI_3$ perovskite solar cells employing nanostructured p-type NiO electrode formed by a pulsed laser deposition. *Adv. Mater.* **2015**, *27*, 4013–4019.
[24] Mitra, R. *Structural Intermetallics and Intermetallic Matrix Composites*; CRC Press: Boca Raton, 2015.
[25] Unutulmazsoy, Y.; Merkle, R.; Fischer, D.; Mannhart, J.; Maier, J. The oxidation kinetics of thin nickel films between 250 and 500 °C. *Phys. Chem. Chem. Phys.* **2017**, *19*, 9045–9052.
[26] Giovanardi, C.; di Bona, A.; Altieri, S.; Luches, P.; Liberati, M.; Rossi, F.; Valeri, S. Structure and morphology of ultrathin NiO layers on Ag(001). *Thin Solid Films* **2003**, *428*, 195–200.
[27] Liu, C.; Huntz, A. M.; Lebrun, J. L. Origin and development of residual stresses in the Ni-NiO system: *In-situ* studies at high temperature by X-ray diffraction. *Mater. Sci. Eng. A* **1993**, *160*, 113–126.
[28] Schade, H.; Smith, Z. E. Mie scattering and rough surfaces. *Appl. Opt.* **1985**, *24*, 3221–3226.
[29] González-Alcalde, A. K.; Méndez, E. R.; Terán, E.; Cuppo, F. L. S.; Olivares, C. J. A.; García-Valenzuela, A. Reflection of diffuse light from dielectric one-dimensional rough surfaces. *J. Opt. Soc. Am. A* **2016**, *33*, 373–382.
[30] Hutchinson, J. W. *Stresses and Failure Modes in Thin films and Multilayers*; Technical University of Denmark: Lyngby, 1996.
[31] Nastasi, M.; Höchbauer, T.; Lee, J. K.; Misra, A.; Hirth, J. P. Nucleation and growth of platelets in hydrogen-ion-implanted silicon. *Appl. Phys. Lett.* **2005**, *86*, 154102.
[32] Lee, J. K.; Lin, Y.; Jia, Q. X.; Höchbauer, T.; Jung, H. S.; Shao, L.; Misra, A.; Nastasi, M. Role of strain in the blistering of hydrogen-implanted silicon. *Appl. Phys. Lett.* **2006**, *89*, 101901.
[33] Jamal, M. S.; Shahahmadi, S. A.; Chelvanathan, P.; Alharbi, H. F.; Karim, M. R.; Dar, M. A.; Luqman, M.; Alharthi, N. H.; Al-Harthi, Y. S.; Aminuzzaman, M. et al. Effects of growth temperature on the photovoltaic properties of RF sputtered undoped NiO thin films. *Results Phys.* **2019**, *14*, 102360.
[34] Mahalingam, T.; John, V. S.; Ravi, G.; Sebastian, P. J. Microstructural characterization of electrosynthesized ZnTe thin films. *Cryst Res. Technol.* **2002**, *37*, 329–339.
[35] Dabrowski, J.; Müssig, H. J. *Silicon Surfaces and Formation of Interfaces: Basic Science in the Industrial World*; World Scientific: Singapore, 2000; pp 414–416.
[36] Tosha, K.; Iida, K. *Residual Stress and Hardness Distributions Induced by Shot Peening*; International Scientific Committee for Shot Peening: Tokyo, Japan, 1990; pp 379–388.
[37] Chen, X.; Vlassak, J. J. Numerical study on the measurement of thin film mechanical properties by means of nanoindentation. *J. Mater. Res.* **2001**, *16*, 2974–2982.
[38] Pharr, G. M.; Oliver, W. C.; Brotzen, F. R. On the generality of the relationship among contact stiffness, contact area, and elastic modulus during indentation. *J. Mater. Res.* **1992**, *7*, 613–617.
[39] Wang, Z. G. Influences of sample preparation on the indentation size effect & nanoindentation pop-in in nickel. Ph.D. Dissertation, University of Tennessee, Knoxville, 2012.
[40] Fasaki, I.; Koutoulaki, A.; Kompitsas, M.; Charitidis, C. Structural, electrical and mechanical properties of NiO thin films grown by pulsed laser deposition. *Appl. Surf. Sci.* **2010**, *257*, 429–433.
[41] De Los Santos Valladares, L.; Ionescu, A.; Holmes, S.; Barnes, C. H. W. Characterization of Ni thin films following thermal oxidation in air. *J. Vac. Sci. Technol. B* **2014**, *32*, 051808.
[42] Zhang, J.; Zhang, L.; Dong, Y.; Li, H. Y.; Tan, C. M.; Xia, G.; Tan, C. S. The dependency of TSV keep-out zone (KOZ) on Si crystal direction and liner material. In *2013 IEEE International 3D Systems Integration Conference*, San Francisco, CA, USA, 2013.